Science Advances

www.advances.sciencemag.org/cgi/content/full/1/3/e1500022/DC1

Supplementary Materials for

Electrically controlling single-spin qubits in a continuous microwave field

Arne Laucht, Juha T. Muhonen, Fahd A. Mohiyaddin, Rachpon Kalra, Juan P. Dehollain, Solomon Freer, Fay E. Hudson, Menno Veldhorst, Rajib Rahman, Gerhard Klimeck, Kohei M. Itoh, David N. Jamieson, Jeffrey C. McCallum, Andrew S. Dzurak, Andrea Morello

Published 10 April 2015, *Sci. Adv.* **1**, e1500022 (2015)
DOI: 10.1126/sciadv.1500022

This PDF file includes:

Supplementary Information

S1 Device Fabrication

The device was fabricated on a 0.9 μm thick epilayer of isotopically purified ^{28}Si, grown on top of a 500 μm thick $^{\mathrm{nat}}$Si wafer. The ^{29}Si has been depleted to 800 ppm in the enriched ^{28}Si epilayer. Single-atom qubits were selected out of a small group of donors implanted in a region adjacent to the Single-Electron-Transistor (SET). In this device, P_2^+ molecular ions were implanted at 20 keV energy in a 100×100 nm^2 window. All other nanofabrication processes were identical to those described in detail in Ref. (*1*), except for a slight modification in the gate layout to bring the qubits closer to the microwave antenna and provide an expected factor $3\times$ improvement in B_1 (see Fig. S2 for schematic of the gate layout).

S2 Experimental Setup

The sample was mounted on a high-frequency printed circuit board in a copper enclosure, thermally anchored to the cold finger of an Oxford Kelvinox 100 dilution refrigerator with a base temperature $T_{\mathrm{bath}} =$ 20 mK. The sample was placed in the center of a wide-bore superconducting magnet, oriented so that the B_0 field was applied along the [110] plane of the Si substrate, and perpendicular to the short-circuit termination of the MW antenna. The magnet was operated in persistent mode while also feeding the nominal current through the external leads. We found that removing the supply current while in persistent mode led to a very significant magnetic field and ESR frequency drift, unacceptable given the intrinsic sharpness of the resonance lines of our qubit. Conversely, opening the persistent mode switch led to noticeable deterioration of the spin coherence, most visible as a shortening of T_2^* in Ramsey experiments.

Room-temperature voltage noise was filtered using an anti-inductively wound coil of thin copper wire with a core of Eccosorb CRS-117 ($\sim$ 1 GHz cutoff), followed by two types of passive low-pass filters: 200 Hz second-order RC filters for DC biased lines, and 80 MHz seventh-order Mini-Circuits LC filters for pulsed voltage lines (see supplementary section S4 for measurements on the frequency response of the SET to a square wave applied to different gates.). The filter assemblies were placed in copper enclosures, filled with copper powder, and thermally anchored to the mixing chamber. DC voltages were applied using optoisolated and battery-powered voltage sources, connected to the cold filter box via twisted-pair wires. Voltage pulses were applied using an arbitrary waveform generator (LeCroy ArbStudio 1104), connected to the filter box via semi-rigid coaxial lines. ESR excitations were generated using an Agilent E8267D analog signal generator, and NMR excitations were produced by an Agilent MXG N5182A vector signal generator. Both excitation signals were combined using a power-combiner and fed to the MW antenna via a CuNi semi-rigid coaxial cable, with attenuators at the 1.5 K stage (10 dB) and the 20 mK stage (3 dB). The SET current was measured by a Femto DLPCA-200 transimpedance amplifier at room temperature, followed by a floating-input voltage post-amplifier, a sixth-order low-pass Bessel filter, and acquired using a PCI digitiser card (AlazarTech ATS9440).

S3 Data Acquisition Statistics

For e^- experiments the state is always initialized spin-down and all of our plots were produced by taking the spin-up proportion from $100 - 200$ single-shot measurement repetitions per point. For ^{31}P experiments, plots were produced by taking the nuclear flipping probability (no initialization to a certain state) from 41 measurement repetitions per point, and 50 electron readouts per nuclear spin readout. See Ref. (*2*) for more details on nuclear spin readout and control sequences.

S4 Frequency Response of the Electrostatic Gates

All electrical gates are low-pass filtered to minimize the electron temperature. The top gate (TG), left barrier gate (LB) and the right barrier gate (RB) are filtered with 200 Hz second-order RC filters. The left donor "slow gate" (LDS) and the right donor "slow gate" (RDS) are filtered with nominally 10 kHz

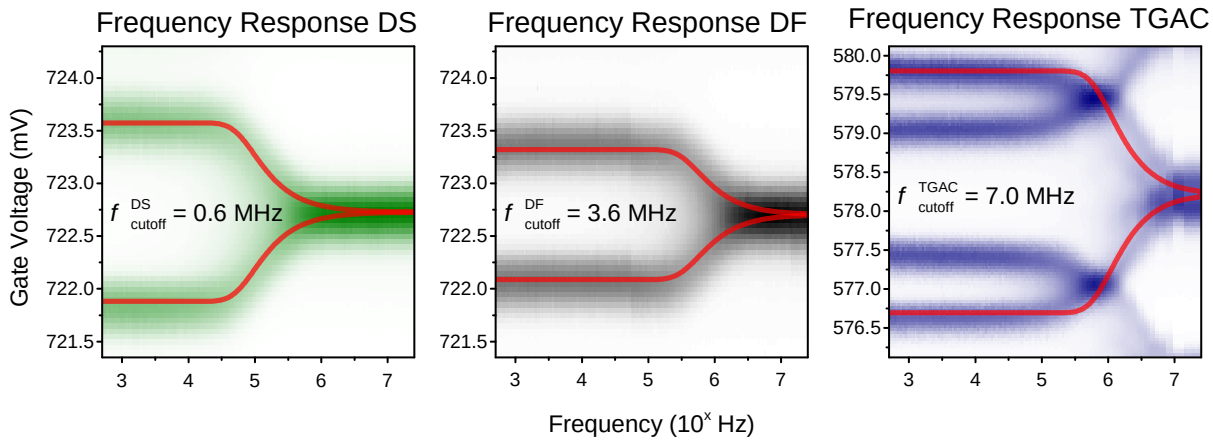

Figure S1: **Frequency response.** Frequency response of the SET current to a square wave applied to donor slow (DS), donor fast (DF) and the SET tuning gate (TGAC). The red solid lines are best estimates of the cutoff frequencies.

second-order RC filters. The left donor "fast gate" (LDF), the right donor "fast gate" (RDF), and the SET tuning gate (TGAC) are filtered with nominally 80 MHz seventh-order Mini-Circuits LC filters (see Fig. S2 for schematic of the gate layout). However, the measured response of the SET to these different gates seems to differ from the engineered cutoffs. The reason for this is unknown, but could be explained by failed components or spurious conducting paths through the copper powder surrounding the lines inside the filter boxes. In Fig. S1 we plot the current through the SET (colored regions indicate higher current) when a square wave is applied to the DS (LDS+RDS), DF (LDF+RDF) and the TGAC gates, respectively. For a frequency below the cutoff of the cable and filter, individual SET Coulomb peaks are split into doublets. Above the cutoff frequencies the square wave is strongly attenuated and the Coulomb peaks merge back into single peaks. We estimate the cutoff frequencies of the different lines by comparing the measured data with theoretically modelled second-order RC filters, where $R_1 = 20$ kΩ, $C_1 = 1$ pF, $R_2 = 20$ kΩ, and $C_2 = 1/(R_2 f_{\mathrm{cutoff}})$. We find $f^{\mathrm{DS}}_{\mathrm{cutoff}} = 0.6$ MHz, $f^{\mathrm{DF}}_{\mathrm{cutoff}} = 3.6$ MHz, and $f^{\mathrm{TGAC}}_{\mathrm{cutoff}} = 7.0$ MHz, and plot the corresponding frequency responses as red lines in Fig. S1.

For the electrically-controlled measurements in the main text, a combination of DS, DF, and TGAC was used as "A-gate". For the measurements in Figs. 2 & S7 the voltages applied to the gates were $V_{\mathrm{DS}} = V_A$, $V_{\mathrm{DF}} = V_A$, and $V_{\mathrm{TGAC}} = 0.8V_A$. For the measurements in Figs. 3 & 4, and all other measurements in the supplementary information we reduced the voltage applied to the DS gate to improve the frequency response of the system. The applied voltages for these measurements were $V_{\mathrm{DS}} = 0.5V_A$, $V_{\mathrm{DF}} = V_A$, and $V_{\mathrm{TGAC}} = 0.8V_A$.

S5 Triangulation of Donor Position

We can triangulate the position of the ion-implanted donor based on the techniques and methods introduced in Ref. (*3*). The triangulation is obtained by combining two different techniques, each one predicting a locus or several loci of donor locations compatible with a measurable physical property of the system. We use a classical, finite-element electrostatic simulation software (TCAD) (*4*), to model the electrostatic potentials in order to match the spin readout criterion (ground state energy of the donor-bound electron aligned with the Fermi level of the SET is-

land), and a geometric capacitance extraction method (FASTCAP) (*5*), to match the measured capacitive coupling between the donor and the surrounding gate electrodes.

For this device, we experimentally observed that the donor was more strongly capacitively coupled to TGAC than to the donor tuning gates LDF, LDF, RDS, and RDF. This indicates that the donor is positioned on the TGAC-side of the SET island. This may be due to misalignment of the implant window during fabrication, or to a donor belonging to the background doping of the epilayer. Matching the relative donor capacitances, obtained from charge stability experiments (see Table 1) with FASTCAP simulations, we obtain 4 loci for the possible donor location (see Figure S2).

A 5th locus can be obtained from matching the spin readout criterion. The device had a threshold voltage of $\sim$ 1.3 V. To faithfully describe the electrostatics of the experimental device, we include a negative interface charge density of $Q_{\mathrm{ox}} = -1.8 \times 10^{12}$ cm^{-2} in the TCAD model, necessary to match the threshold voltage (*3*). This charge density is consistent with estimates from deep level transient spectroscopic measurements (*6*). In a gated nanostructure, the donor can be susceptible to strain which

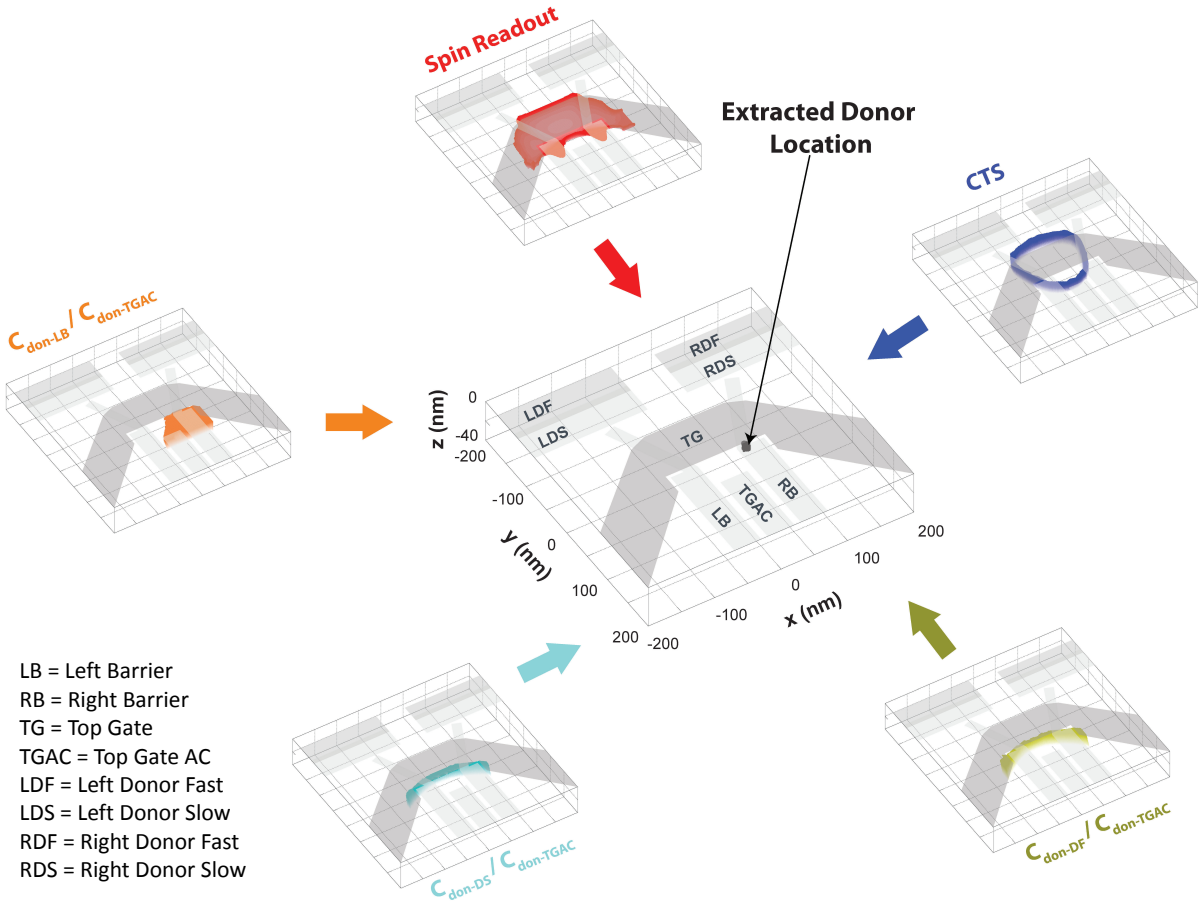

Figure S2: **Donor triangulation.** Donor position extracted from a combination of donor ground state energy and relative donor capacitances to various gates. The combination of donor capacitances and spin readout criterion aids to reduce the uncertainty of the donor position to ± 4, ± 2.5 and ± 3.5 nm in the three cartesian axis x, y and z.

Gates	Relative Capacitance
$C_{donor-\mathrm{LB}}/C_{donor-\mathrm{TGAC}}$	0.65± 0.25
$(C_{donor-\mathrm{LDS}}+C_{donor-\mathrm{RDS}})/C_{donor-\mathrm{TGAC}}$	1.53± 0.25
$(C_{donor-\mathrm{LDF}}+C_{donor-\mathrm{RDF}})/C_{donor-\mathrm{TGAC}}$	0.36± 0.075
$CTS = C_{donor-island}/C_{donor}$	0.36± 0.06

Table S1: Relative gate capacitances used for triangulation of the donor position.

can modify the conduction band energy (*7*, *8*). Therefore, for our metrology, we choose a fairly large error bar for the spin readout criterion, accepting locations with $E_c = 45.6 \pm 20$ meV. The locus that matches the spin readout criterion is plotted in Fig. S2. We will see in Section S6 that the electric field at our final donor location is ~ 6 MV/m, resulting in a slope of the conduction band of ~ 6 meV/nm. Hence, our large error bar in the spin readout criterion would only translate to a small error in donor position of ~ 3 nm.

The 5 shells in Fig. S2 intersect to within a region [50 ± 4, -31.5 ± 2.5, -8.5 ± 3.5], and represent the possible set of donor locations in the device. The donor is located under the right barrier gate RB, towards the TGAC gate.

S6 Electric Field Simulations

We can use the triangulated donor positions and our TCAD model of the Si/SiO_2 structure with the Al-gates (see section S5) to estimate the local electric field at the donor site. Fig. S3 shows the magnitude and direction of the calculated electric field for $V_A = 50$ mV (additional to $V_{\mathrm{LB}} = 0.92$ V, $V_{\mathrm{RB}} = 0.92$ V, $V_{\mathrm{TG}} = 1.798$ V, $V_{\mathrm{DS}} = 0.579$ V, $V_{\mathrm{DF}} = 0.575$ V, $V_{\mathrm{TGAC}} = 0.45$ V, compare also with section S4) inside a coordinate range that comprises the triangulated donor positions.

Since the donor is located beneath the barrier gate, the positive bias applied to this gate ($V_{\mathrm{RB}} = 0.92$ V) causes the electric field to point in negative z-direction, and the electron wavefunction is pulled towards the interface and away from the nu-

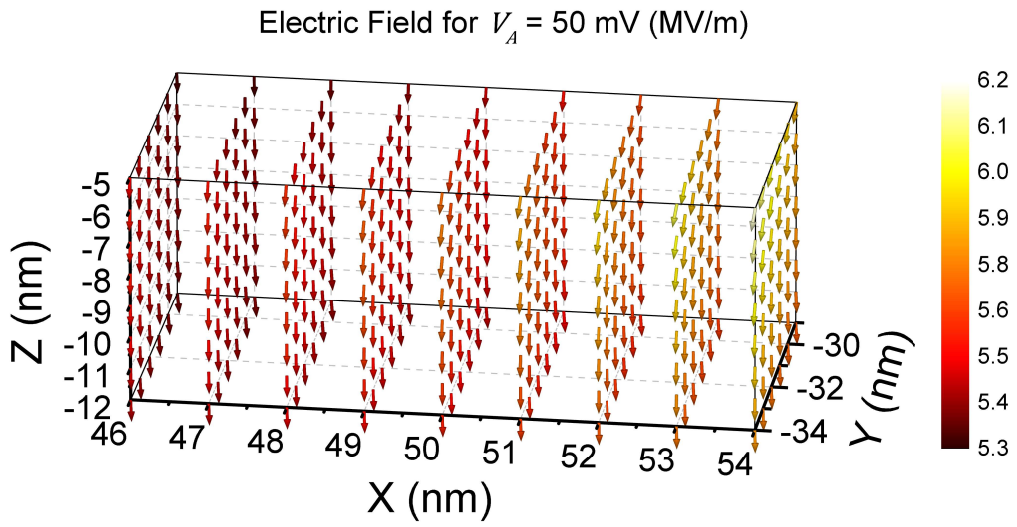

Figure S3: **Electric field simulations.** Calculated electric field for $V_A = 50$ mV.

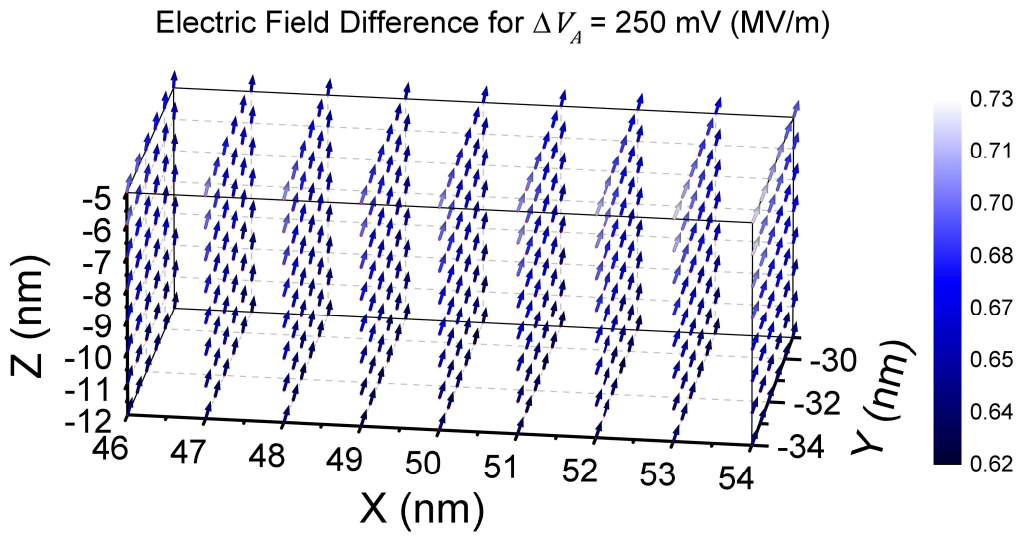

Figure S4: **Electric field simulations.** Calculated electric field difference for $\Delta E = E_{V_A=300\mathrm{mV}} - E_{V_A=50\mathrm{mV}}$.

cleus. This explains the very low initial hyperfine coupling $A = 96.9$ MHz, which is significantly different from the bulk value of 117.53 MHz. Increasing V_{RB} should pull the electron even further away from the nucleus reducing A even more. This means that we are starting in a situation slightly different from what is schematically depicted in Fig. 1B, as the electron is already displaced towards the interface from the beginning.

It may seem contradictory that, in experiment, we have measured a positive tuning parameter $\alpha_A = 0.91 \pm 0.07$ MHz/V, meaning that a more positive V_A leads to an increase in the hyperfine coupling. This is explained by the fact that the A-gate consists of the DS-gates, DF-gates, and the TGAC-gate (see section S4), which are all located some distance away from the donor. In this case an increase in V_A will effectively compensate the electric field under the right barrier. We confirm this in Fig. S4, where we plot the change in electric field when V_A is increased from $V_A = 0.50$ mV to $V_A = 300$ mV, i.e. $\Delta V_A = 250$ mV. The change in electric field is clearly positive, reducing the magnitude of the vertical electric field when V_A is increased, and therefore pushing the electron back towards the donor, resulting in a positive value of α_A.

In Fig. S5 we plot the electric field E at possible donor locations as a function of V_A. The stars correspond to the compensated plunge position ("Pulse ESR/NMR" position in Fig. 2A), that keeps the potential of the SET island constant with respect to the Fermi level of source and drain (*9*, *1*). The diamonds correspond to the electric fields calculated for the different values of V_A. The absolute value of E varies significantly between the different donor positions, and converting V_A into E would be subject to a large error. However, the tunability of E is very similar for all locations. Therefore, we fit this set of simulations to extract an average value for the tunability $dE/dV_A = -2.62(5)$ MVm^{-1}/V, where the error is the standard deviation of the slopes of individual fits. This value is used to convert from V_A to dE with good accuracy, and to calculate the "Electric Field Change"-axis of Fig. 2B.

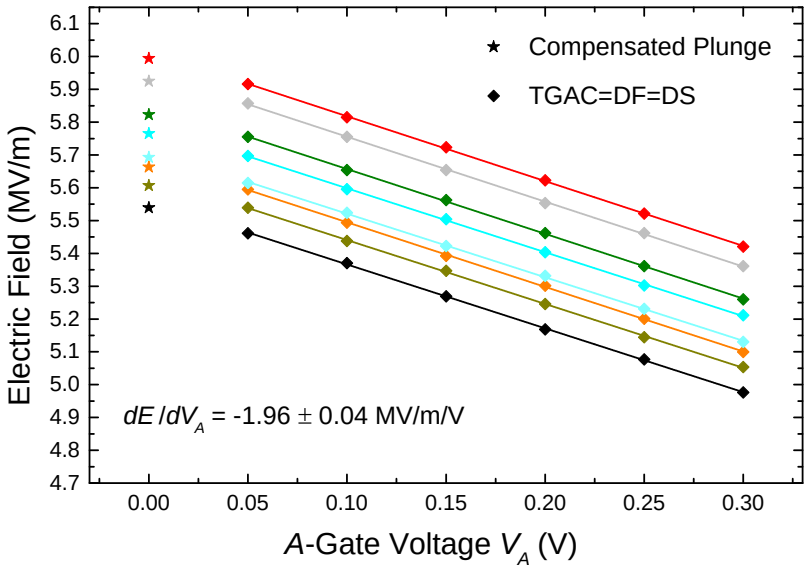

Figure S5: **Electric field simulations.** Calculated electric field as a function of V_A for possible donor locations. The change in electric field is very similar for all donor locations.

S7 Atomistic Simulations of the Hyperfine Coupling

The spin Hamiltonian of a ^{31}P donor electron spin **S** and nuclear spin **I** in an electrostatic potential ϕ and magnetic field $\mathbf{B}_0$ is given by:

$$H_{\mathrm{P-spin}} = \gamma_e(\phi)\mathbf{S}\cdot\mathbf{B}_0 - \gamma_n\mathbf{I}\cdot\mathbf{B}_0 + A(\phi)\mathbf{I}\cdot\mathbf{S}$$

The first and second terms in Equation S7 are the electronic and nuclear Zeeman terms, the third term is the contact hyperfine interaction between the two spins, and γ_e and γ_n are the electron and nuclear gyromagnetic ratios, respectively. The contact hyperfine coupling (*10*) is expressed as $A(\phi) = \frac{8\pi}{3}\gamma_e(\phi)\gamma_n|\psi(r_0,\phi)|^2$, where $|\psi(r_0,\phi)|^2$ is the probability density of the electron wave function evaluated at the donor site r_0.

The relative tunability of the gyromagnetic ratio $\alpha_{\gamma_e}/\gamma_e(0)$ is two orders of magnitude smaller than the relative tunability of the hyperfine coupling $\alpha_A/A(0)$ (refer to Fig. 2 and Ref. (*11*)). The hyperfine coupling relative to the bulk value ($A(0) = 117.6$ MHz) can, therefore, be approximated as (*3, 12, 13*)

$$\frac{A(\phi)}{A(0)} = \frac{|\psi(r_0,\phi)|^2}{|\psi(r_0,0)|^2}. \qquad (2)$$

We use a numeric implementation of tight binding - packaged as a software tool called NanoElectronic MOdeling-3D (NEMO-3D) (*14, 15*) - to calculate the hyperfine coupling of the donor at the location triangulated in Section S5 and for the electric fields simulated in Section S6. Typical simulation domains of 30 nm $\times$ 30 nm $\times$ 30 nm consisting of approximately 1.4 million atoms were considered. Each NEMO simulation with the above domain takes $\sim$ 2 hours, when run on a computing cluster with 48 processors.

In Fig. S6A we plot the calculated hyperfine coupling for $V_A = 50$ mV for three different donor depths d at the triangulated position. Confinement by the interface enhances $|\psi(r_0,\epsilon)|^2$ beyond the bulk value for near shallow donors ($d = 4.3$ nm), resulting in a hyperfine coupling greater than 117.6 MHz. However, for donors further away from the inter-

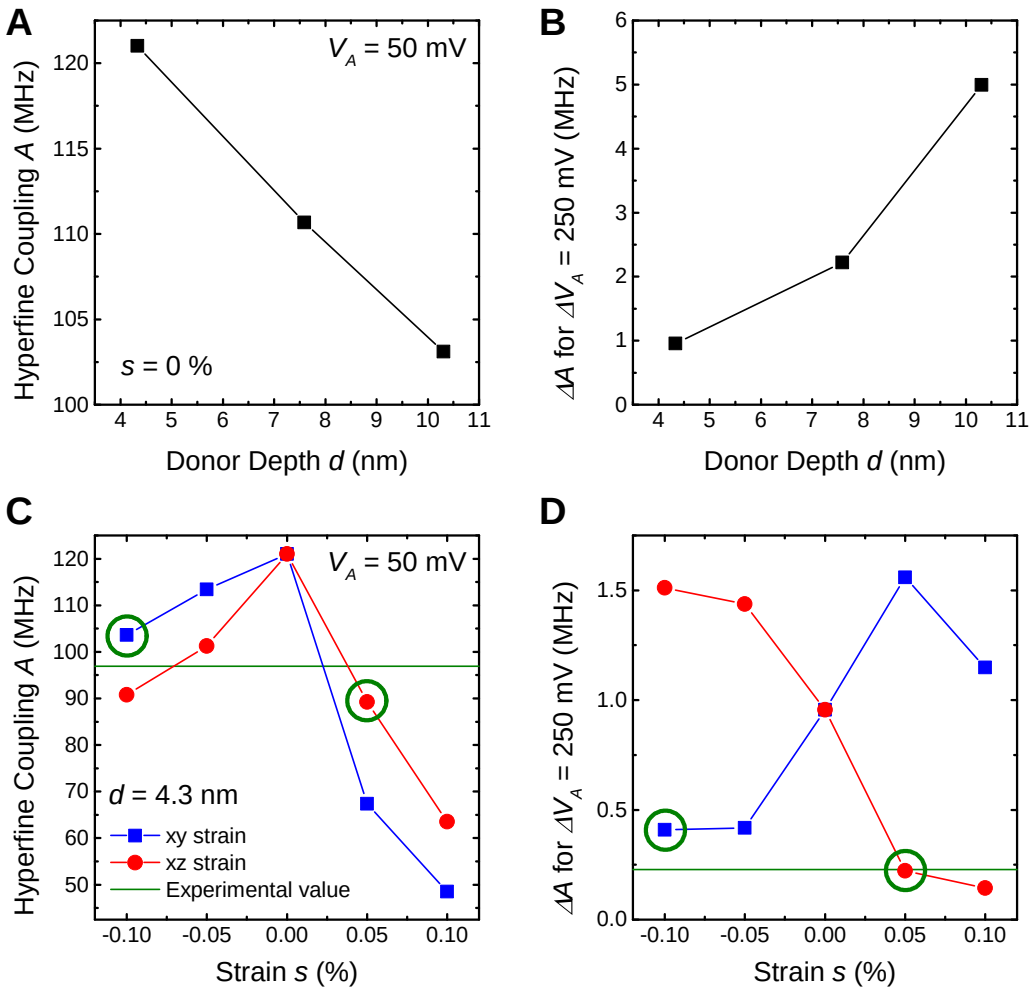

Figure S6: **Atomistic tight binding simulations of the hyperfine coupling for a donor at the location determined in section S5, for the electric fields simulated in section S6, and subject to lattice strain. A, B** Hyperfine coupling and tunability of the hyperfine coupling as a function of donor depth under the SiO_2 in the unstrained lattice. **C, D** Hyperfine coupling and tunability of the hyperfine coupling as a function of lattice strain for a donor depth $d = 4.3$ nm under the SiO_2. The green lines indicate the experimental values and the green circles highlight simulations in good agreement with the experimental results.

face, the electric field pulls the electron away from the nucleus, resulting in a decrease in hyperfine coupling (*13, 16*). The tunability of the hyperfine coupling ΔA, i.e. how strongly A is modified when the electric field is changed, scales inversely proportional with the confinement of the electron. We plot $\Delta A = A_{V_A=300\mathrm{mV}} - A_{V_A=50\mathrm{mV}}$ for three different donor depths in Fig. S6B. We notice that the calculated tunability of A is much larger than the experimentally measured one (compare Fig. 2). We believe this to be due to strain of the Si lattice, which also influences the hyperfine coupling by distorting the donor wave function (*17*).

We cannot quantify the strain in our device, but Thorbeck *et al.* (*7*) estimate that strain due to metal surface gates in nanoelectronic devices can be as

much as ~ 0.1 %. Especially with the donor located directly under a barrier gate (see supplementary section S5) we expect significant strain at the donor location. We repeat the hyperfine calculations for the donor $d = 4.3$ nm below the interface for different values of homogeneous strain. Here, compressive strain ($s < 0$) in the xy-plane will lead to tensile strain ($s > 0$) in the z-direction. We plot the calculated hyperfine coupling for $-0.1\% < s < 0.1\%$ for strain applied to the xy-plane (blue squares) and the xz-plane (red circles) in Fig. S6C ($V_A = 50$ mV). Any type of strain decreases the wavefunction overlap of electron and nucleus and reduces the hyperfine coupling A. In Fig. S6D, we plot the corresponding tunability of the hyperfine coupling ΔA (for $\Delta V_A = 250$ mV). For certain values of s both the absolute value of A and the tunability ΔA are in good agreement with the experimental values of $A_{exp} = 96.9$ MHz and $\Delta A_{exp} = 0.228$ MHz (highlighted with green circles). While the presence of strain in the device seems to be able to match the simulated values with the experimental values, we cannot conclusively attribute the observed effects to a specific value of strain. Further and more detailed simulations would be required to untangle the effects of electric field, strain and the SiO_2 interface on the hyperfine coupling.

Electric fields, strain and the SiO_2 interface have profound consequences for future multi-qubit devices as they can lead to a strong variability in the hyperfine coupling A and, therefore, to distinctively different qubit resonance frequencies. It can, however, be expected that multi-qubit devices with deterministically positioned donors will have a smaller variability in the hyperfine coupling as the donors can be placed at locations with little or at least similar strain. Furthermore, a gate layout optimized for maximizing the Stark shift should give a tunability of the resonance frequencies of a few MHz and be sufficient for the operation of a multi-qubit quantum computer with a monochromatic global microwave field. In a scenario where the variability is too large or the tuning range too small, the global microwave could be operated as multi-tone continuous-wave driving field at regular frequency spacing.

S8 Electron Spin Resonance Spectrum & Rabi Oscillations - Experiment & Theory

In Fig. S7B we show a gate-controlled measurement of the ESR spectrum, obtained by shifting ν_e with V_A. The nuclear spin is in the $|\Uparrow\rangle$ state for the duration of the experiment, and we apply a continuous-wave MW driving field at frequency $\nu_{\mathrm{MW}} = \nu_{e2}^{\mathrm{ref}} - 200$ kHz. Here, ν_{e2}^{ref} is the ESR frequency for $|\Uparrow\rangle$ obtained from a conventional pulsed Ramsey experiment at the compensated plunge position ("Pulse ESR/NMR" position in Fig. 2A). We start the sequence (see Fig. S7A) at $V_A = 0$ V to load an electron in the $|\downarrow\rangle$ state by spin-dependent tunneling (*9*) ("Read/Init." position in Fig. 2A). We then apply a positive V_A pulse to shift $\nu_{e2}(V_A)$ towards ν_{MW} for the duration t_p, which results in a coherent manipulation of the spin. We then pulse V_A back to 0 V to perform single-shot readout of the electron spin (*9*), and we repeat the whole sequence 200 times to extract the electron spin-up fraction $P_\uparrow(V_A)$. For $V_A = V_r \approx 155$ mV, an increased count of spin $|\uparrow\rangle$ electrons indicates that $\nu_{e2}(V_A)$ becomes resonant with the MW source. By optimizing the duration of the gate pulse we can ensure that the electron spin undergoes a π-rotation while on resonance, yielding $P_\uparrow \approx 1$.

The maximum $P_\uparrow$ occurs at a frequency shift $\Delta\nu_e = -217$ kHz instead of the expected -200 kHz. This shift and the presence of side lobes at larger V_A, is caused by the finite time response of the electrical control gates, which are low-pass filtered to minimize electron heating (see supplementary section S4 for details). When measuring the gate-controlled ESR spectrum beyond ν_{MW} ($V_A > V_r$), we sweep $\nu_{e1}(V_A)$ through the resonance and back again. The limited bandwidth of the gates causes slow crossings through the resonance condition, resulting effectively in a Landau-Zener-Stückelberg interferometry experiment (*18*). Time-evolution simulations of the whole sequence (red line in Fig. S7B), taking into account the bandwidths of the different gates, show excellent agreement with the measured data. In a setup optimized for electrical control, the rise-time of the A-gate should be chosen much shorter than the qubit

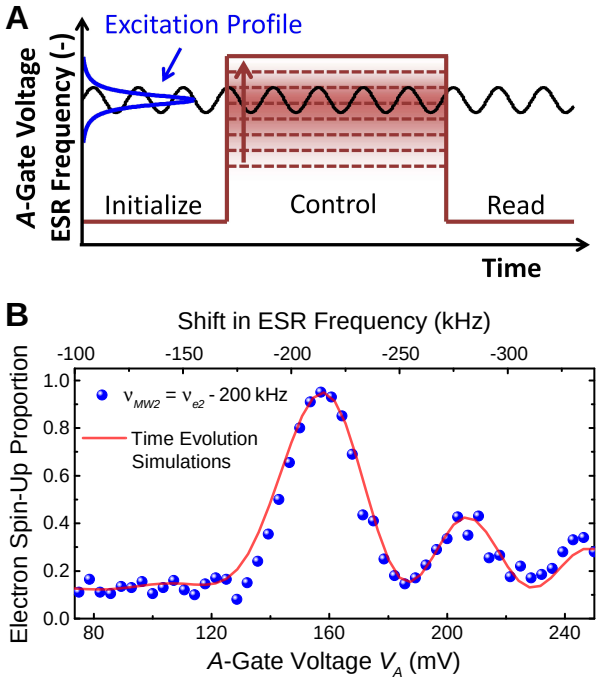

Figure S7: **Electrically controlled ESR spectrum. A**, Schematic of the sequence used to measure the electrically controlled ESR spectrum. **B**, ESR spectrum obtained by electrically tuning the ESR transition (for $|\Uparrow\rangle$) in resonance with the continuous-wave MW source ($\nu_{\rm MW} = \nu_{e2} - 200$ kHz) with a short voltage pulse. Time evolution simulations (red line) are in excellent agreement with the data.

Rabi period while on resonance.

In the following paragraphs we present the theoretical model that we have set up to describe the temporal response of the donor system to a voltage pulse on the A-gate, and the temporal evolution of spin qubits when they are tuned into resonance with a CW magnetic driving field.

We model the experimental data using the density matrix formalism with the Hamiltonian

$$H(t) = \frac{1}{2}h\Delta\nu(t)\sigma_z + \frac{1}{2}h\Omega_0\sigma_x, \qquad (3)$$

where $\Delta\nu(t) = \nu_{e2}(t) - \nu_{\rm MW}$ is the detuning between the ESR transition and the MW source, and $\Omega_0 = 23.8$ kHz is the Rabi frequency for a $B_1 = 0.85$ μT, which gives a π-pulse length of 21 μs. The output power of the MW source $P_{\rm MW} = -22$ dBm was chosen very low for these experiments to reduce the power broadening of the ESR line. The dephasing time $T_2 = 970$ μs of the electron spin (see Fig. 3H) is included in the master equation of the Lindblad form (*19*)

$$\frac{d\rho}{dt} = -\frac{i}{\hbar}[H,\rho] + \mathcal{L}(\rho), \qquad (4)$$

where

$$\begin{aligned}\mathcal{L}(\rho) &= \frac{1}{2T_2}\left(2\sigma_z\rho\sigma_z - \sigma_z\sigma_z\rho - \rho\sigma_z\sigma_z\right)\\ &= -\frac{2}{T_2}\sigma_x\rho. \qquad (5)\end{aligned}$$

We then use the equation of motion (4) to numerically compute the time evolution of an electron initialized in $|\downarrow\rangle$.

From the measurements in Fig. 2B, we know $d\nu_{e2}/dV_A$ and can allocate the total shift in ν_{e2} to DS, DF, and TGAC in accordance to their respective relative capacitive couplings to the donor (see section S5)

and temporally filtered to their respective cutoff frequencies (see section S4). This allows us to generate the detuning trace $\Delta\nu(t)$ for any measurement and detuning sequence that we want to model:

$$\begin{aligned}\Delta\nu(t) &= \frac{(d\nu_{e2}/dV_A)}{C_{donor-\mathrm{DS}}/C_{donor-\mathrm{TGAC}} + C_{donor-\mathrm{DF}}/C_{donor-\mathrm{TGAC}} + 1} \\ &\quad \left((C_{donor-\mathrm{DS}}/C_{donor-\mathrm{TGAC}})V_A^{\mathrm{DS}}(t) + (C_{donor-\mathrm{DF}}/C_{donor-\mathrm{TGAC}})V_A^{\mathrm{DF}}(t) + V_A^{\mathrm{TGAC}}(t)\right) \\ &= \frac{-1.36\ \mathrm{MHz/V}}{1.53 + 0.36 + 1}\left(1.53V_A^{\mathrm{DS}}(t) + 0.36V_A^{\mathrm{DF}}(t) + V_A^{\mathrm{TGAC}}(t)\right).\end{aligned}$$

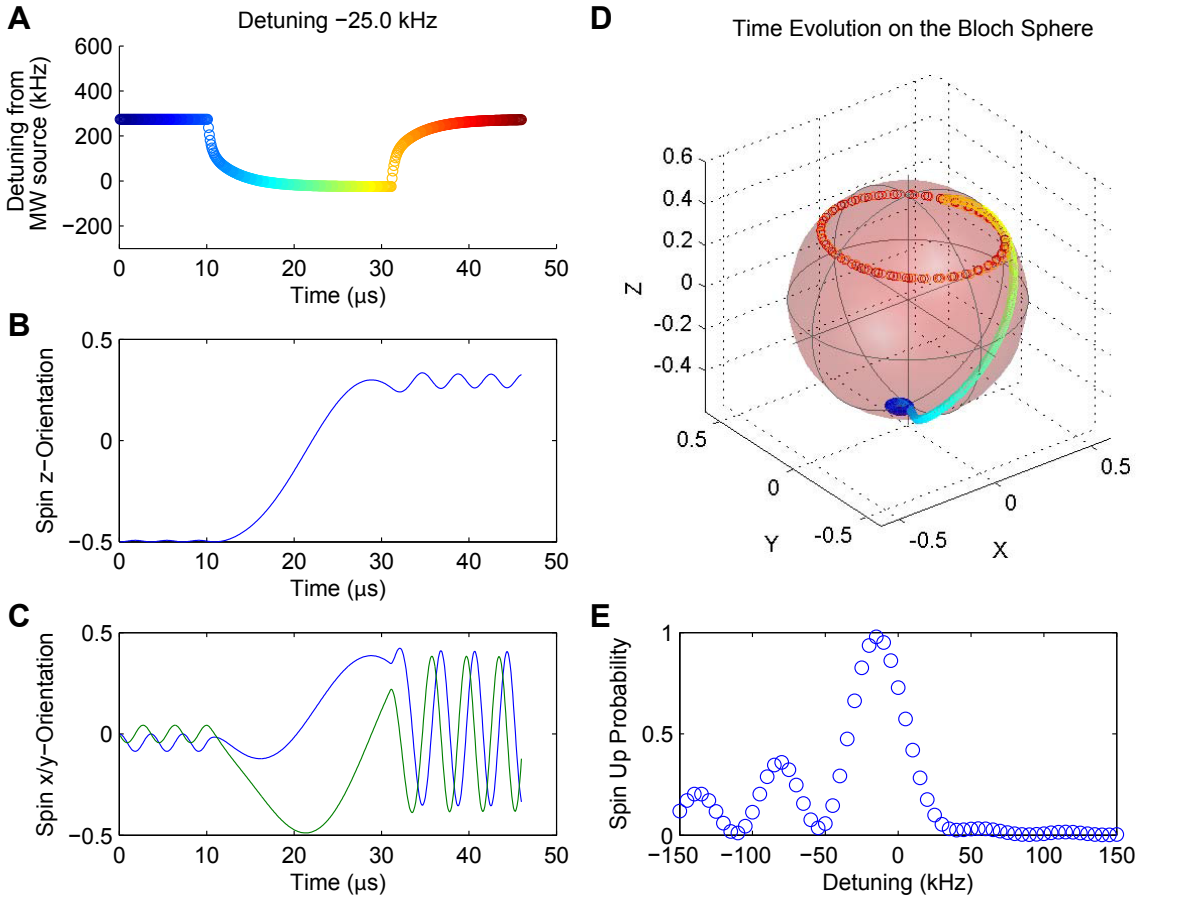

Figure S8: **Time evolution simulations of the electrically controlled ESR spectrum.** Simulations depicting the time evolution of the electron spin around the Bloch sphere for a detuning pulse of $t_{pulse} = 21\ \mu$s and amplitude 249 kHz that tunes the ESR transition to 25 kHz lower frequency than the MW drive.

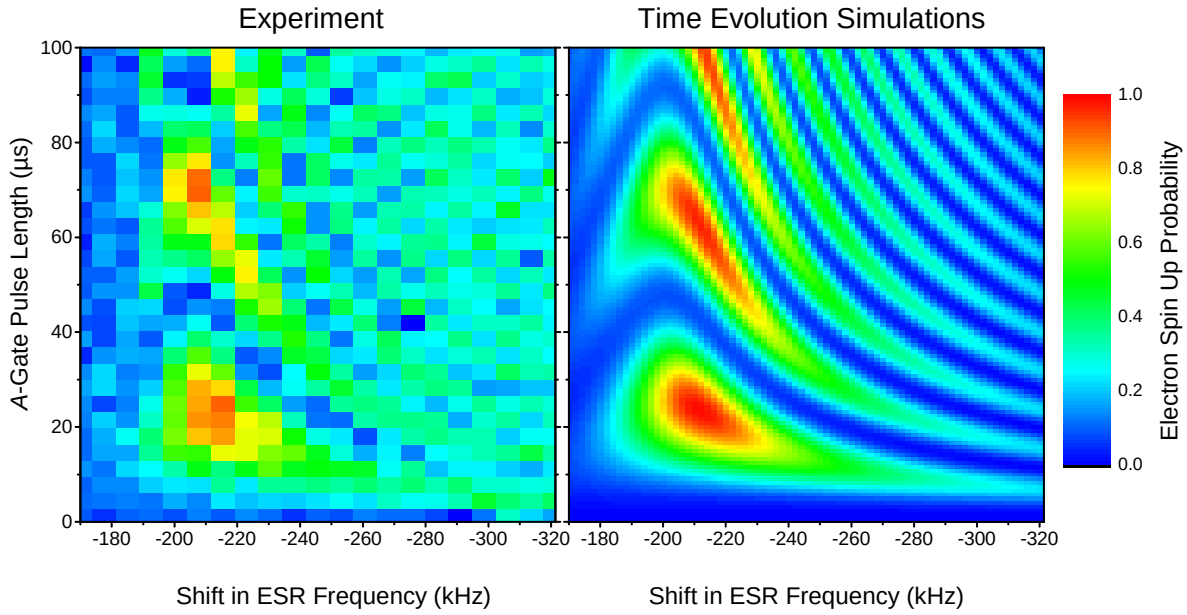

Figure S9: **Electrically controlled Rabi spectrum.** Experimental data and time evolution simulations on the electrically controlled Rabi spectrum.

Here, $V_A^{\mathrm{DS}}(t)$, $V_A^{\mathrm{DF}}(t)$, and $V_A^{\mathrm{TGAC}}(t)$ are the low-pass filtered ($f_{\mathrm{cutoff}}^{\mathrm{DS}} = 0.6$ MHz, $f_{\mathrm{cutoff}}^{\mathrm{DF}} = 3.6$ MHz, and $f_{\mathrm{cutoff}}^{\mathrm{TGAC}} = 7.0$ MHz) voltage traces that are applied to the gates.

Fig. S8A shows $\Delta\nu(t)$ for an electrically-controlled ESR measurement. The time evolution

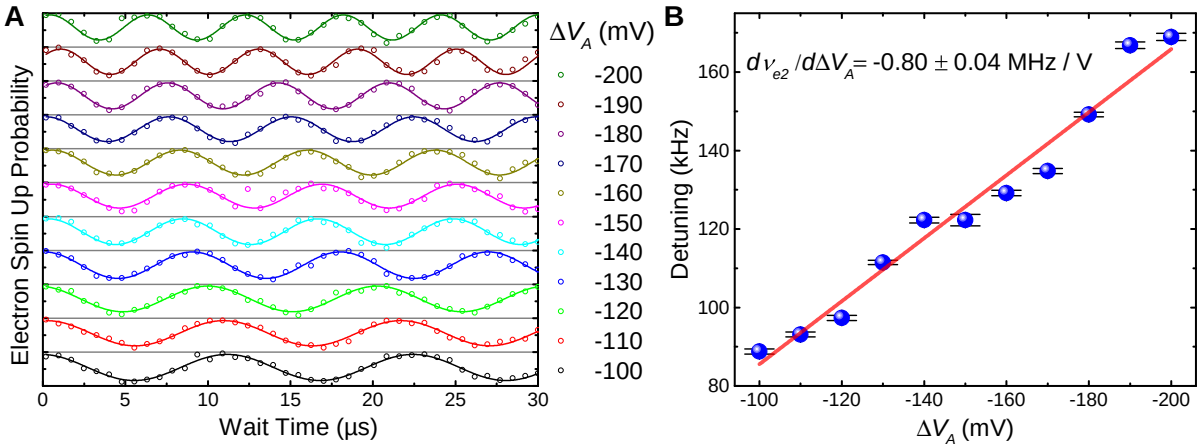

Figure S10: **Electrically controlled electron Ramseys.** **A** Set of EC Ramsey experiments for different voltage pulses ΔV_A conducted on the e^-. **B** Corresponding frequency shift as a function of ΔV_A.

simulation starts with an electron in the $|\downarrow\rangle$ state at $\Delta\nu = 274$ kHz for the first 10 μs. $\Delta\nu$ is then changed to -25 kHz (in this specific example) for a time of $t_{pulse} = 21$ μs (π-pulse) before it is tuned back to 274 kHz for 16 μs. Fig. S8B,C,D show the time evolution of the electron spin during this sequence. The final z-orientation of the electron spin is then plotted in Fig. S8E, and the whole calculation is repeated for different detuning values to build up the entire ESR spectrum (comp. Fig S8E and Fig. S7B). The calculated spectrum is in very good agreement with the experimental data when taking into account non-unity readout fidelity (0.85 %) and non-zero background counts (0.12). The sidelobes at $\Delta\nu < 0$ are well reproduced. They appear when ν_{e2} is tuned through ν_{MW} at the beginning of the pulse and back at the end. The limited bandwidth of the A-gate causes slow crossings through the resonance condition, resulting effectively in a Landau-Zener-Stückelberg (LZS) interferometry experiment (*18*).

The measurements of Fig. S7B and the calculations of Fig. S8 can be also be performed as an electrically-controlled Rabi experiment, where the final electron spin orientation is measured as a function of the length of the voltage pulse. In Fig. S9 we plot the experimentally determined, electrically-controlled Rabi spectrum in the left panel, and the simulated one in the right panel. Again, the simulations are in excellent agreement with the experimental data and the evolution of the LZS sidelobes is well reproduced.

S9 Ramsey Experiments

The ability to apply $V_A(t)$ sequences to the A-gate allows us to perform arbitrary qubit control sequences as already demonstrated in Fig. 3 and Fig. 4. This supplies us with an alternative way to measure the frequency shift induced by V_A. While the measurement in Fig. 2B was conducted changing V_A during the control phase and pulsing the MW source, we can also conduct an electrically-controlled Ramsey experiment as introduced in Fig. 3D. In Fig. S10A we plot a series of Ramsey measurements, where $\Delta V_A = V_A^{\mathrm{wait}} - V_A^{\mathrm{pulse}}$, i.e. the detuning of the spin transition during the wait time, was changed from one measurement to the next. The frequency of the Ramsey oscillations corresponds to the detuning, and we plot the extracted values as function of ΔV_A in Fig. S10B. The slope of the linear fit is $d\nu_{e2}/d\Delta V_A = -0.80 \pm 0.04$ MHz/V.

Fig. S11 shows a similar data set for the ^{31}P neutral nucleus. The slope of the linear fit is $d\nu_{n1}/d\Delta V_A = 0.30 \pm 0.01$ MHz/V, which allows us to calculate the tuning parameters $\alpha_A = dA/d\Delta V_A = 2d\nu_{n1}/d\Delta V_A = 0.60 \pm 0.02$ MHz/V, and $\alpha_{\gamma_e} B_0 = d\gamma_e B_0/d\Delta V_A = d\nu_{e2}/d\Delta V_A - d\nu_{n1}/d\Delta V_A = -1.10 \pm 0.05$ MHz/V, with $\alpha_{\gamma_e} = d\gamma_e/d\Delta V_A = -0.71 \pm 0.04$ MHz/V/T at $B_0 = 1.55$ T. All the values extracted in this section are

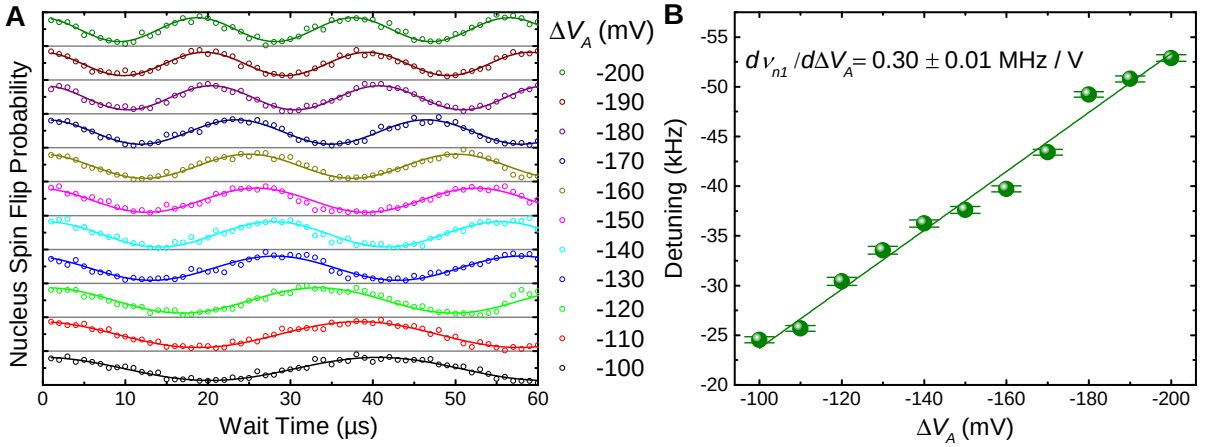

Figure S11: **Electrically controlled nuclear Ramseys. A** Set of EC Ramsey experiments for different voltage pulses ΔV_A conducted on the ^{31}P neutral nucleus. **B** Corresponding frequency shift as a function of ΔV_A.

slightly smaller than the values extracted from Fig. 2. This is because we reduced the voltage applied to the DS gate ($V_{\mathrm{DS}} = 0.5V_A$ compared to $V_{\mathrm{DS}} = V_A$ for the measurements in Fig. 2) to improve the frequency response of the system for all electrically-controlled measurements involving pulsing sequences (see also section S4).

S10 Coherence Times Measurements

In addition to the Hahn echo and CPMG measurements introduced and presented in Fig. 3G,J,K, we performed Ramsey experiments to extract T_2^* and dynamical decoupling experiments with a different number of refocussing pulses. The result of these measurements is presented in Fig. S12 for the e^- and in Fig. S13 for the ^{31}P neutral nucleus. Furthermore, the measurements on the e^- have been performed as both electrically controlled and conventional, pulsed spin resonance experiments to directly compare these two measurements methods. The Ramsey experiments are displayed in Fig. S12A,B, the measured CPMG decay traces and their fits are displayed in Fig. S12C,D and Fig. S13A, and the extracted decay times are plotted as a function of number of CPMG pulses in Fig. S12E,F and Fig. S13B.

The electron spin coherence times obtained for electrically controlled and pulsed experiments are identical within the error bars, indicating that there is no additional source of decoherence introduced by performing electrically-controlled measurements. The free induction decay time is $T_2^* = 220\mu s$ (see Fig. S12A,B) and the extended coherence times reach values of $T_{2e}^{\mathrm{CPMG}} = 10$ ms for 32 decoupling pulses (see Fig. S12C-F) for both experimental methods. The electron spin coherence times can be fitted with

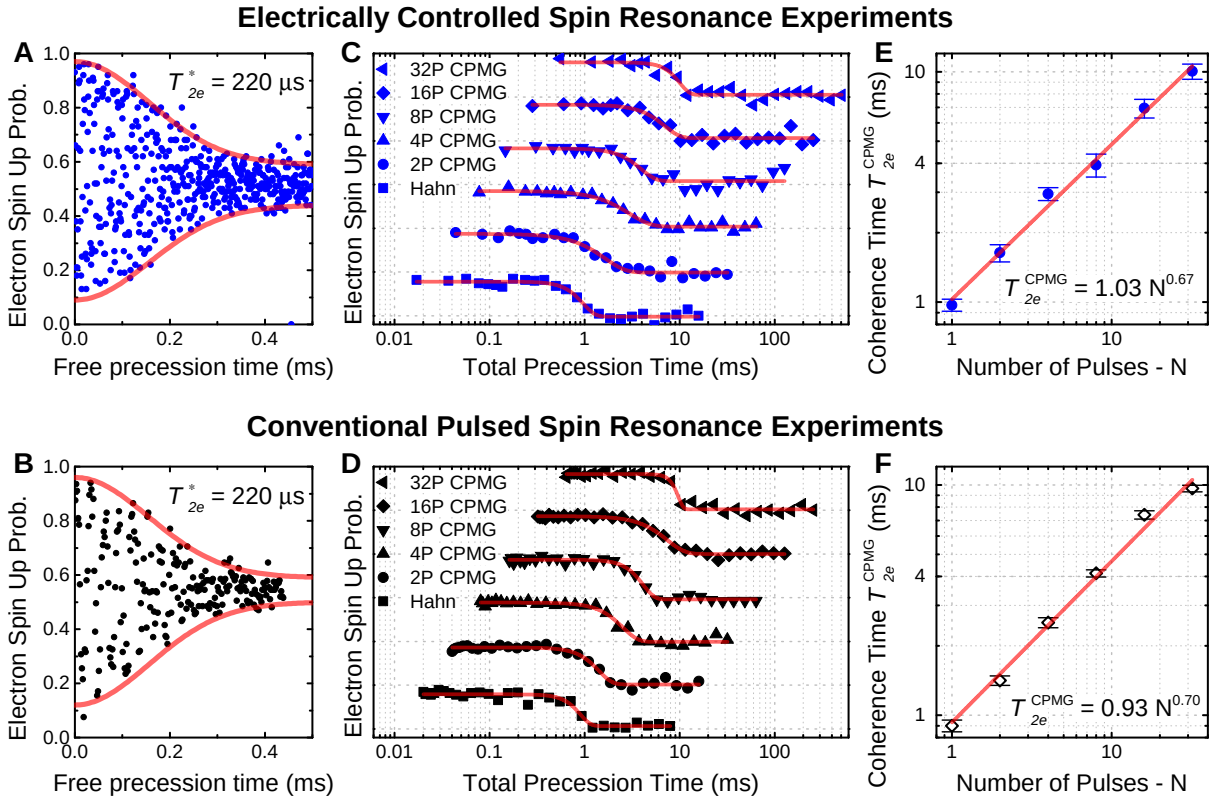

Figure S12: **Electrically controlled electron coherence times. A,B** Ramsey experiments to extract T_2^* for the electron qubit. **C,D** CPMG dynamical decoupling decay traces for different numbers of refocussing pulses. **E,F** Extracted coherence times T_{2e}^{CMPG} as a function of number of refocussing pulses N.

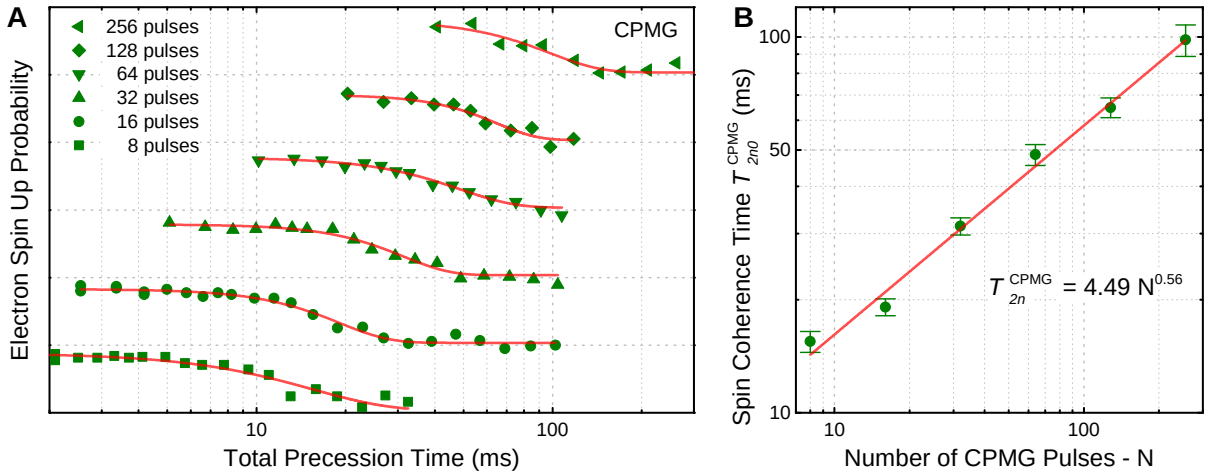

Figure S13: **Electrically controlled nuclear coherence times. A** Set of EC CPMG dynamical decoupling performed on the ^{31}P neutral nucleus. **B** Extracted coherence times T_{2n}^{CPMG} as a function of number of decoupling pulses.

$T_{2e}^{\mathrm{CPMG}} \propto N^{\alpha/(\alpha+1)} = N^{0.67}$, where $\alpha = 2.0$ gives information about a colored noise spectrum with $S(\omega) \propto 1/\omega^{2.0}$ in good agreement with the data obtained by noise spectroscopy with pulsed-MW control sequences with $T_{2e}^{\mathrm{pulseCPMG}} = 0.93N^{0.70}$ ($\alpha = 2.3$). This is another strong indicator, that the electrically-controlled measurements do not introduce significant additional noise.

The coherence times of the neutral nucleus can be fitted with $T_{2n}^{\mathrm{CPMG}} \propto N^{\alpha/(\alpha+1)} = N^{0.56}$, with $\alpha = 1.3$ that hints towards $1/f$-type noise. In contrast to the measurements presented here, in measurements with pulse-RF control sequences we were not able to significantly extend T_{2n}^{CPMG} with dynamical decoupling sequences (see Ref. (*20*)). We believe that this is caused by a sensitivity of the donor system to the RF radiation, possibly by a process as simple as heating. For the pulse-RF technique, the RF power was chosen higher and pulsing of the RF source will lead to a non-equilibrium state. On the other hand for the electrically-controlled technique, the RF power was chosen lower (to reduce power broadening of the NMR transition) and the CW RF drive was leading to a steady-state situation.